

激光选区熔化 DD91 镍基单晶高温合金的单道形貌、晶体取向和微观组织

李继康¹, 张振武¹, 杨源祺¹, 蔡超¹, 李伟^{2,3,4**}, 魏青松^{1*}

¹华中科技大学材料科学与工程学院材料成形与模具技术国家重点实验室, 湖北 武汉 430074;

²武汉科技大学冶金装备及其控制教育部重点实验室, 湖北 武汉 430081;

³武汉科技大学机械传动与制造工程湖北省重点实验室, 湖北 武汉 430081;

⁴武汉科技大学精密制造研究院, 湖北 武汉 430081

摘要 采用激光选区熔化成形了 DD91 镍基单晶高温合金的单条熔道,研究了激光功率和扫描速度对单道形貌、晶体取向和微观组织的影响规律。结果表明:当铺粉层厚为 30 μm 时,在激光功率 290~305 W、扫描速度 500~700 mm/s 工艺窗口内,熔道连续平稳且光滑平直,熔池扁平规则,可为单晶组织的稳定生长提供保障。当熔池与单晶基板冶金良好时,熔池内晶体能够延续基板的取向沿[001]定向外延生长,但熔池对流可使晶体生长方向产生 2°以内的小角度偏差,并在熔池顶部发生柱状晶向等轴晶的转变,产生杂晶缺陷。熔池底部、两侧和中部都存在大量沿[001]生长的柱状枝晶,一次枝晶臂间距为 0.6~0.8 μm ,实现了沿单晶基板的外延生长,但中部晶体形态转变为纺锤状;熔池顶部晶粒为细小胞状结构,生长方向由[001]转变为[100],这主要是顶部凝固时热量更多地沿扫描方向(平行于基板)传递导致的。研究结果可为激光增材制备大尺寸单晶组织提供参考。

关键词 激光技术;激光选区熔化;DD91 合金;镍基单晶高温合金;单道;晶体取向;微观组织

中图分类号 TG146.1

文献标志码 A

DOI: 10.3788/CJL202249.1402103

1 引言

镍基单晶高温合金是航空航天领域的关键材料,主要用于发动机热端涡轮叶片的制造。镍基单晶高温合金减少了晶界强化元素,与常规等轴晶和柱状晶相比,具有优异的高温持久、抗高温氧化、抗高温蠕变的性能,大大提高了涡轮叶片的使用寿命和使用温度。目前,常用定向凝固和精密铸造的方法制备此类组织/零件,如高速凝固(high rate solidification, HRS)、液态金属冷却(liquid metal cooling, LMC)等,通过水或液态金属等强制冷却的方法在熔体中建立特定方向的温度梯度,从而控制凝固传热的方向,促进晶体的定向生长。较大的温度梯度是单晶组织制备的关键,现有技术下温度梯度为 30~100 K/cm^[1]。当温度梯度较低时,容易出现枝晶组织粗大、雀斑、杂晶、元素偏析等缺陷^[2-3]。但受加热技术的限制,现有温度梯度难以有大幅度的提高,要使其有新的飞跃,必须改变热源或加工方式^[1]。此外,单晶涡轮叶片的空心薄壁复杂结构对制备工艺也提出了更为严苛的要求,传统定向凝固

工艺难以满足单晶高温合金的应用需求。

激光选区熔化(selective laser melting, SLM)是基于粉末床的金属增材制造技术,以激光为热源,逐点逐道逐层熔化微细金属粉末,能够实现任意复杂结构的近净成形^[4]。当枝晶能够按一致取向外延生长时,就意味着单晶的制备成功^[5]。大量研究证明,SLM能够实现晶体的外延生长,故在制备单晶组织甚至涡轮叶片方面具有一定的潜力。这是由于激光光斑小(80~150 μm),热密度高,熔池内部温度梯度可达 10³~10⁵ K/cm^[6],高出传统定向凝固 1~3 个数量级,并且凝固速率高达 10⁵~10⁷ K/s^[7],几乎无宏观偏析缺陷;其次,激光定向能量具有明显的方向性传热特点,熔池凝固的热量可沿熔池向基板的路径定向散失^[8]。上述优势为熔池内晶体的定向外延生长提供了有利的冶金条件。

目前,国内外针对 SLM 制备单晶组织的研究鲜有报道,大多数集中于激光熔融沉积(laser melting deposition, LMD)的方式。相比 SLM, LMD 的激光光斑大(1~3 mm),熔池宽深比大,稳定性高,但成形

收稿日期: 2021-12-20; 修回日期: 2022-01-08; 录用日期: 2022-01-26

基金项目: 国家自然科学基金(51905193, 51775207)、湖北省重点研发计划项目(2020BAB049)、华中科技大学学术前沿青年团队项目(2017QYTD06)、中央高校基本科研业务费专项资金(2021yjsCXC028)

通信作者: *wqs_xn@163.com; **lwliwei1989@163.com

精度低,难以制备出复杂精细结构。如 Wang 等^[9]使用 LMD 制备出尺寸为 18 mm×10 mm×23 mm 的 SRR99 单晶合金试样,并建立了防止再结晶的热处理制度。Liang 等^[10-11]利用 LMD 制备出约 7 mm 高的 René N5 单晶组织,并发现高冷却速率可减少低熔点 γ - γ' 共晶组织的产生。Pan 等^[12-13]利用 SLM 制备出 2 mm 高的 SRR99 单晶组织,并通过数值模拟计算方法验证了 SLM 制备单晶的理论可行性。综上,利用激光来制备单晶组织具有一定的可行性,且部分学者已初步制备出小尺寸的单晶组织,但该方面的研究仍十分有限。上述研究可为理解 SLM 制备单晶组织提供有益的借鉴和参考。

SLM 是逐点连接、逐道搭接和逐层堆积的成形方式,单道熔池是其成形过程的最小单元,所以研究单条熔道的形貌、晶体取向和微观组织具有一定的工程意义。本文使用不同的工艺参数成形了 DD91 第四代镍基单晶高温合金的单条熔道,分析了激光功率和扫描

速度对单道几何特征、晶体取向和微观组织的影响规律,并进一步探讨了裂纹、杂晶等缺陷的产生机理,为 SLM 制备大尺寸单晶组织提供了理论和技术参考。

2 实验方法

2.1 实验材料

成形材料选用雾化制备的 DD91 第四代单晶高温合金粉末,基板材料选用定向凝固铸造并经热处理的 SRR99 第一代单晶高温合金棒材(端面直径为 16 mm,长度为 150 mm),均由中国科学院金属研究所提供。两种合金的名义化学成分如表 1 所示,相比 SRR99 合金,DD91 合金添加了抗高温的 Re、Ru 等贵金属元素,并提高了固溶强化元素 Co 的含量,以此降低 γ' 强化相的长大速率,形成高密度的位错网,进而增强材料的热稳定性并增大材料的持久强度和蠕变抗力等。粉末的微观形貌和粒径分布分别如图 1(a)、(b)所示,可以看出粉末球形度较高,少量颗粒表面粘

表 1 SRR99 和 DD91 高温合金的名义化学成分(质量分数,%)

Table 1 Nominal chemical compositions of SRR99 and DD91 superalloys (mass fraction, %)

Element	Co	Cr	W	Ta	Al	Ti	C	Ni
SRR99 substrate	5.000	8.400	9.500	2.800	5.500	2.100	0.015	Bal.
Element	Co	Cr+W+Mo+Ta	Re	Ru	Al	Hf	Ni	
DD91 powder	12.0	19.0	5.4	3.0	5.8	0.1	Bal.	

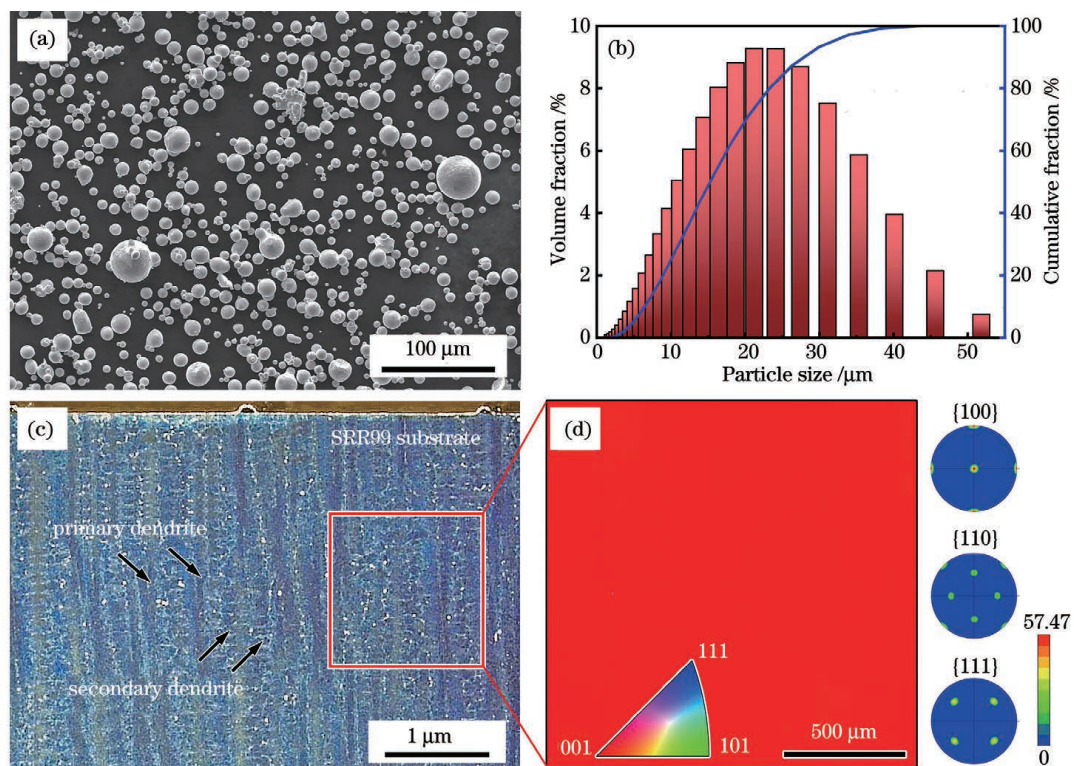


图 1 雾化 DD91 高温合金粉末和 SRR99 基板的 EBSD 晶体取向测试结果。(a) 粉末形貌;(b) 粉末粒径分布;(c) 基板侧面的光镜形貌;(d) 晶体取向图和极图

Fig. 1 Gas-atomized DD91 superalloy powder and EBSD crystal orientation result of SRR99 substrate. (a) Morphology of powder; (b) particle size distribution of powder; (c) OM morphology of side substrate; (d) crystal orientation map and pole figure

附卫星球,粒径为 $8.6\sim 37.5\ \mu\text{m}$,平均值为 $20.4\ \mu\text{m}$ 。实验前,将粉末置于烘箱中, $80\ ^\circ\text{C}$ 静置 $10\ \text{h}$ 以去除水分,提高铺粉过程中粉末的流动性。SRR99 基板侧面的微观形貌如图 1(c)所示,可以看到一次枝晶均沿垂直方向生长,枝晶间距为 $250\sim 350\ \mu\text{m}$,并且有较多的二次枝晶臂。此外,使用电子背散射衍射 (electron backscattered diffraction, EBSD) 技术检测基板的晶体取向,如图 1(d)所示,可以看出,所检测区域整体呈现红色,意味着晶体沿 $[001]$ 方向定向生长,并且极图表明其具有明显的 $\{100\}\langle 001\rangle$ 立方织构,最大极密度达到了 57.47 ,满足实验条件。实验时,利用镍基单晶合金的外延生长特性,在此基板 (001) 晶面上进行 SLM 成形实验。

2.2 实验设备与工艺

成形设备使用自主搭建的 SLM150 装备,配备了锐科 $500\ \text{W}$ 连续单模光纤激光器,激光光斑聚焦后直径约为 $100\ \mu\text{m}$ 。实验前,使用线切割将 SRR99 单晶

棒切割成 5 个 $\Phi 16\times 5\ \text{mm}$ 的圆柱,圆柱上下表面作为 SLM 成形面,经砂纸打磨,随后在超声波清洗机中除去磨屑等杂质颗粒,烘干后当作基板备用。

SLM 成形单道示意图如图 2(a)所示,在 SRR99 单晶基板 (001) 晶面上铺设 $30\ \mu\text{m}$ 厚的 DD91 合金粉末,随后激光按设定的工艺参数依次成形出单道。成形的工艺参数如下:激光功率为 $245\sim 305\ \text{W}$,扫描速度为 $500\sim 1100\ \text{mm/s}$,成形腔内通入氩气以避免氧化。5 个单晶基板分别对应 5 个不同的激光功率,在每个基板依次成形出 7 条不同扫描速度的熔道,如图 2(b)所示,相邻道间距为 $2\ \text{mm}$,最终成形出 35 条 $10\ \text{mm}$ 长的不同工艺参数的单道试样,如图 2(c)所示。实验中定义激光的线能量密度为

$$\eta = \frac{P}{v}, \quad (1)$$

式中: η 为线能量密度 ($\text{J}\cdot\text{m}^{-1}$); P 为激光功率 (W); v 为扫描速度 ($\text{m}\cdot\text{s}^{-1}$)。

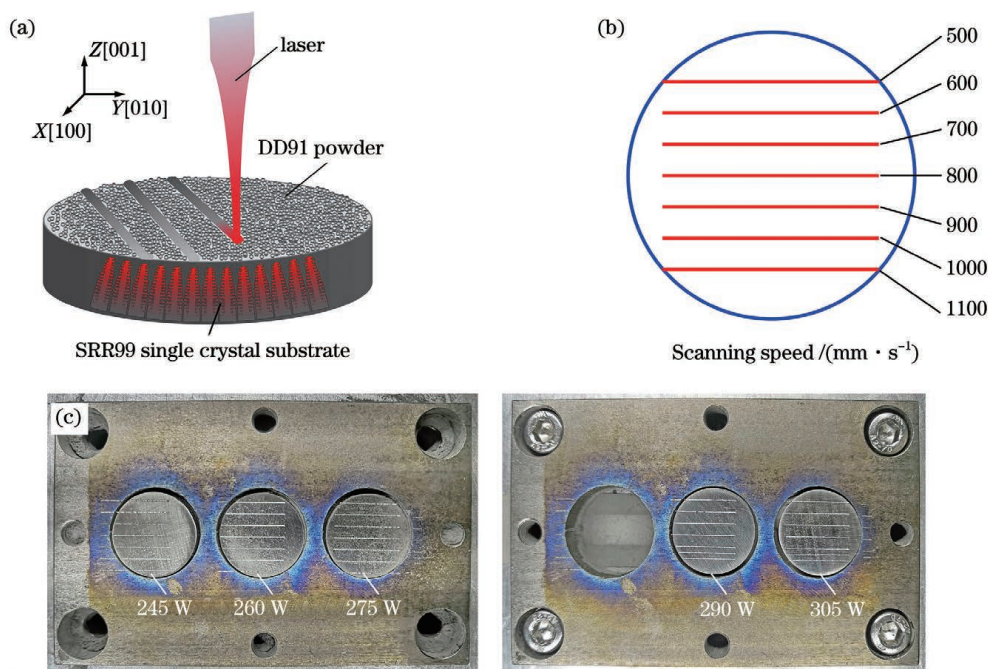


图 2 SLM 单道成形示意图和单道试样。(a)单道激光扫描示意图;(b)单道成形参数设置;(c)不同工艺参数下制备的单道试样

Fig. 2 Schematic of SLM single-track forming and single-track samples. (a) Schematic of single-track laser scanning; (b) parameter setting of single-track forming; (c) single-track samples fabricated under different process parameters

2.3 表征设备与方法

成形后,使用线切割将基板纵向剖开,经磨抛后观察单道熔池的显微形貌和晶体取向。使用 A2 电解液对熔池进行电解抛光,在 $20\ \text{V}$ 起始电压下作用 $10\ \text{s}$,以满足后续检测表征。使用光镜 (OM) 观察熔道的表面形貌,评价成形质量;使用场发射扫描电镜 (SEM) 观察粉末、熔池等微观形貌和组织;使用 ImageJ 图像处理软件对熔池的几何特征尺寸进行测量分析;使用电子背散射衍射分析晶体取向,扫描步长为 $0.25\ \mu\text{m}$,并使用 AztecCrystal 软件处理采集的数据。

3 结果与讨论

3.1 单道形貌

图 3 为 35 条不同参数下熔道表面的光镜形貌图。每条熔道左边标有线能量密度 η ($\text{J}\cdot\text{m}^{-1}$),右上角标“▲”表示成形质量较好的熔道,其轮廓清晰,连续平整,无明显氧化,表面有明显的金属光泽。通过 η 可以进一步评价熔道的特征,可以看出,当 η 过低时,熔道不连续,部分粒径较大粉末难以完全熔化,且在强烈对流和表面张力的作用下,出现较多球化缺陷;当 η 适中时,粉末能够吸收充足热量,被加热至熔点和沸点之

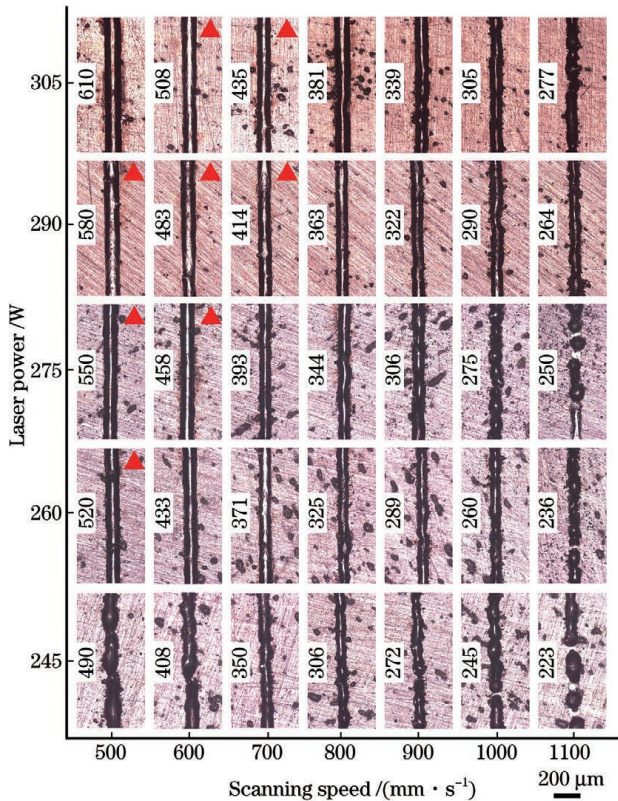


图3 不同工艺参数下成形的熔道光镜形貌

Fig. 3 OM morphologies of single-tracks under different process parameters

间,保证了其充分熔化,又不至于汽化,熔道质量较好;当 η 过高时,熔道两侧及表面发黑,由于温度过高,甚

至超过熔体沸点,产生过烧,不利于熔道的连续性和稳定性。并且已有大量文献对此进行了深入研究^[14-16],在此不再过多赘述。综上可得,在铺粉层厚为 $30\ \mu\text{m}$ 下,当线能量密度 η 为 $414\sim 580\ \text{J}\cdot\text{m}^{-1}$ 时,能够获得优异的DD91合金熔道。

图4为激光功率为290 W时不同扫描速度下熔道的电镜形貌图。可以看到,随着扫描速度的增大,激光对粉末的冲击力增大,粉末被冲散,使得熔道表面的起伏加剧,宽度不均匀,如图4(a)所示。此外,当扫描速度为1000 mm/s和1100 mm/s时,产生了与扫描方向相垂直的裂纹,贯穿整条熔道,并且裂纹断面暴露了树枝晶结构,留下了较宽的不规则裂缝,这属于典型的凝固裂纹的特征,如图4(b)~(d)所示。这些裂纹的产生可能有两方面原因。

其一,材料因素。为提高蠕变抗性,高温合金中加入了大量的Al或Ti,以保证含有 $40\%\sim 80\%$ (质量分数)的 γ' -Ni₃(Al, Ti)金属间化合物。然而,有研究表明,当Al和Ti含量(质量分数)超过4.5%时,合金就具有较高的热裂纹敏感性,具有不可焊接性^[17]。本实验选用的DD91合金的Al名义含量(质量分数)高达5.8%,在 γ 相凝固时,Al将不断被排斥到液相中产生局部富集,这种溶质偏析能够降低局部液相线温度,并在枝晶间产生富集Al溶质原子的液膜,此外激光的高温梯度容易诱导局部热应力集中^[18],液膜在热应力作用下被拉开,导致开裂,这在其他 γ' 强化型高温合金的激光加工中也常常出现,难以避免^[19-20]。

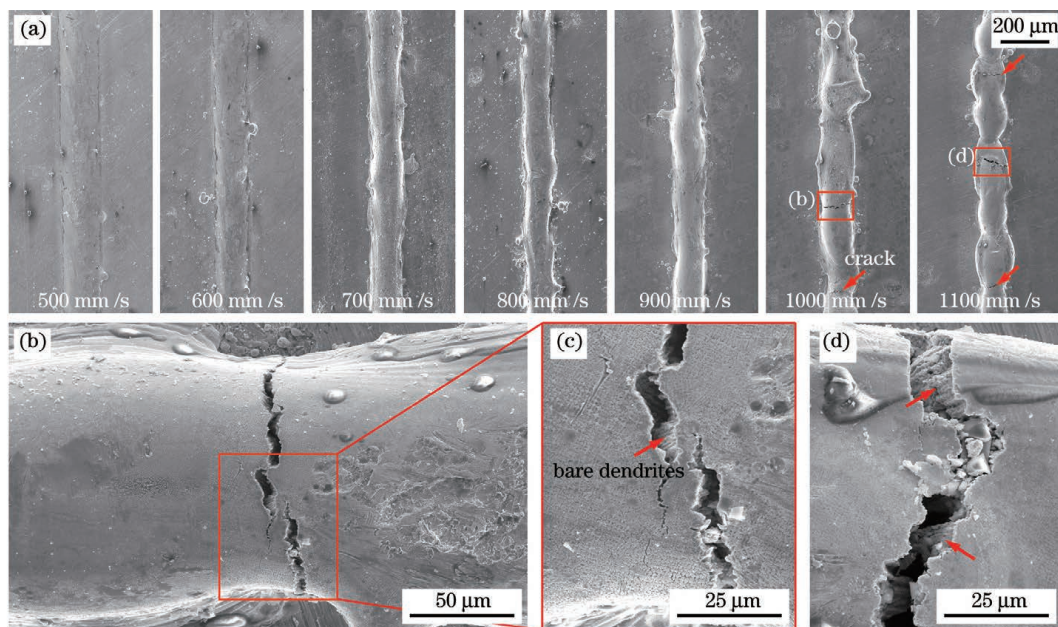


图4 激光功率为290 W时不同扫描速度下成形的熔道形貌。(a)熔道形貌;(b)~(d)裂纹形貌

Fig. 4 Morphologies of single-tracks under different laser scanning speeds at laser power of 290 W. (a) Morphologies of single-tracks; (b)~(d) morphologies of cracks

其二,工艺因素。当扫描速度过快时,线能量密度低,激光与合金粉末的作用时间短,难以将其完全熔化,熔池中熔体少且流动性差,没有足够的熔体及时弥

补凝固收缩的空隙;此外,凝固速率也随扫描速度的增大而增大,凝固收缩引起的局部应力较大,使枝晶间液膜更容易被撕裂^[21]。因此,应选择合适的工艺参数

(如较低的扫描速度), 尽可能避免此类缺陷。

图5为不同参数下熔池截面的电镜形貌图。右上角标有“▲”的熔池形状较为规则, 类似于传统焊接时焊缝的不对称双弧状。此类熔池是在高功率、低速度下成形的, 激光与粉末作用时间长, 热量积累较多, 降低了熔池的表面张力, 使其在基板上更容易铺展, 熔池的尺寸也随之增大。此类熔池的宽深比较大, 其温度梯度方向更接近于 $[00\bar{1}]$, 更利于单晶组织的外延生

长。然而在245 W的激光功率下, 熔池呈现半圆形或球冠形, 这是由于输入能量较低, 基板熔透深度浅, 熔池难以与其冶金结合, 并且温度低的熔体表面张力大, 与基板的润湿效果差, 难以铺展开来, 产生了球化缺陷。这将对熔池的温度梯度的方向性造成不利影响, 晶体也难以获得并延续基板的 $[001]$ 取向生长。综上, 高功率、低速度下熔池的形状更加规则稳定, 能为单晶的外延生长提供良好的几何条件。

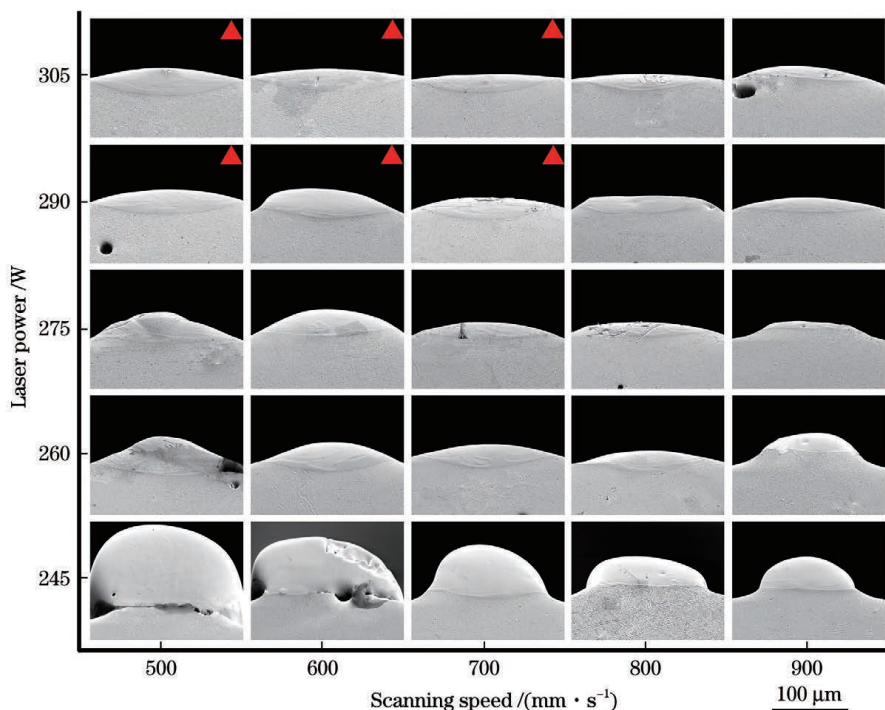


图5 不同工艺参数下成形的熔池截面形貌

Fig. 5 Cross-sectional morphologies of molten pools under different process parameters

图6为不同工艺参数下熔池的几何特征统计图, 其中 w 为熔池的宽度, h 为熔池的整体高度, θ 为熔池边缘与基板的接触角。可以发现, 当功率相同时, 随扫描速度的增大, 熔池的宽度、深度、接触角和面积均降低, 但宽深比随之增大, 这是由于高速度的线能量密度低, 热量的输入减少, 并且激光与粉末的作用时间缩短, 热量的传递时间也减少, 最终熔化的范围变小。其次, 当扫描速度相同时, 随功率的增加, 激光熔透基板的深度增加(即凹陷程度变大), 但宽度、高度和面积变化均较小, 即不同功率下的熔池尺寸特征相差不大, 这主要是由于增加的热输入大部分用于抵消合金的蒸发潜热, 熔池的传热主导类型也由热传导(凹陷程度小的熔池)转变为蒸发散热(凹陷程度大的熔池)^[22]。综合以上分析, 在铺粉层厚为 $30\ \mu\text{m}$ 下, 设置合理的激光功率和扫描速度, 如在激光功率为 $290\sim 305\ \text{W}$ 、扫描速度为 $500\sim 700\ \text{mm/s}$ 的工艺窗口内, 可以获得连续平稳、光滑平直、没有裂纹的熔道, 其熔池也更加扁平规则, 自上而下的传热特性更为显著, 能为单晶组织的稳定生长提供保障。

3.2 晶体取向

图7为不同工艺参数下熔池截面的晶体取向结果。根据图2(d)的晶体取向图例, 不同的颜色代表不同的晶体取向, 红色代表沿 $\langle 001 \rangle$ 生长的晶体。结果显示, 熔池的形状对晶体取向的影响差异性较小, 大部分熔池内的晶体表现出很明显的择优取向, 即能够延续单晶基板的取向, 沿 $[001]$ 定向外延生长。已有研究证实, 晶体的实际生长方向取决于温度梯度的方向与择优取向的方向两者的夹角, 晶体将选择与热流方向最为接近的择优取向进行生长^[23]。镍基高温合金具有面心立方(FCC)的晶体结构, 其非密排面的生长速率比密排面更快^[24], 使得晶核更容易沿 $\langle 001 \rangle$ 方向择优生长。此外, 激光扫描过程中, 基板温度较低, 凝固热量可由熔池向基板快速散失, 热流呈现近似自上而下的单方向性。所以, 当在单晶基板的 (001) 晶面上扫描时, 熔池内晶体生长速度最快的方向恰好与热量散失的方向互相平行, 为晶体沿基板的 $[001]$ 外延生长提供了条件。

图8列出了三种有代表性的晶体缺陷, 进一步分

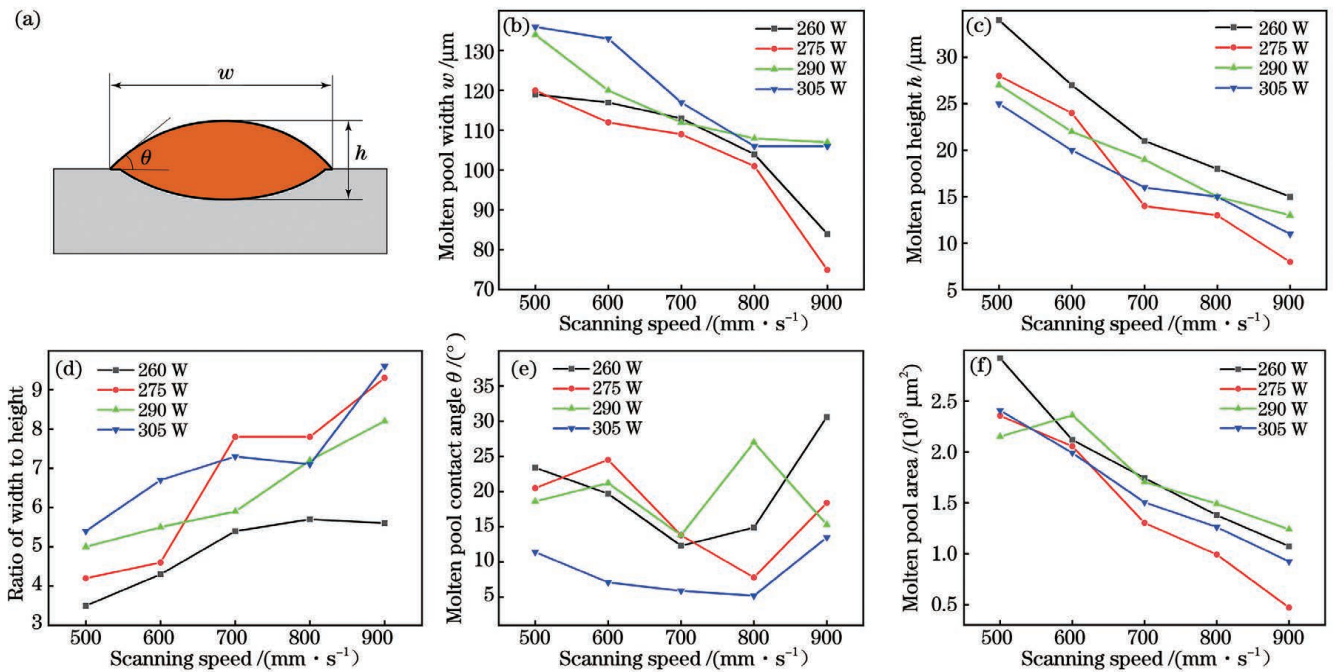


图6 熔池示意图和熔池特征尺寸与工艺参数的关系。(a)熔池示意图;(b)熔池宽度;(c)熔池高度;(d)熔池宽高比;(e)熔池接触角;(f)熔池面积

Fig. 6 Schematic of molten pool and relationship between molten pool feature sizes and process parameters. (a) Schematic of molten pool; (b) molten pool width; (c) molten pool height; (d) ratio of molten pool width to height; (e) contact angle; (f) molten pool area

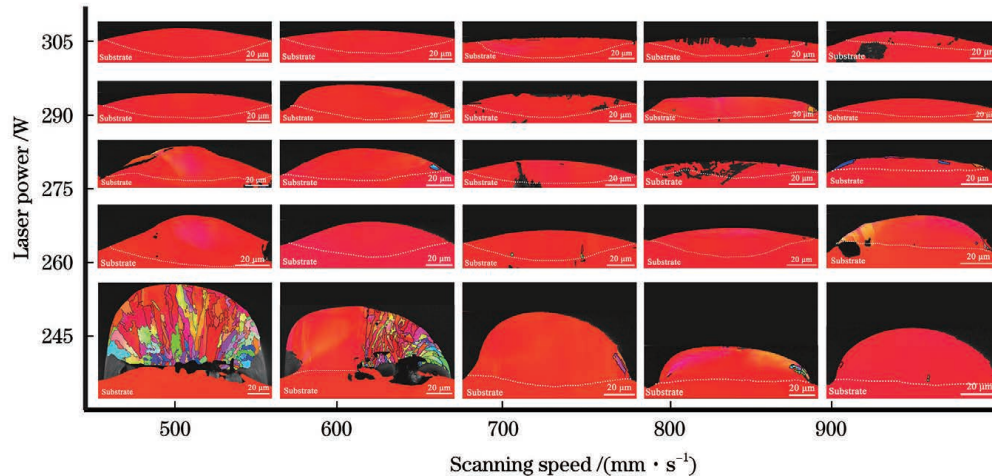


图7 不同工艺参数下成形的熔池 EBSD 晶体取向测试结果

Fig. 7 EBSD crystal orientation results of molten pools formed under different process parameters

析其形成机理。可以发现,缺陷主要包含三类:其一,熔池内部晶粒生长杂乱,如图8(a)所示;其二,少部分晶粒取向发生小角度偏移,产生了取向偏差,直观上看晶粒取向图颜色由红色转变为橙色或粉红色,如图8(c)所示;其三,熔池顶部和两侧出现杂散等轴晶粒等,如图8(d)所示。

针对第一类缺陷,图8(b)展示了点A到点B的相邻像素点取向差,可以发现,当熔池与基板之间的冶金结合较好时,晶体延续了基板的取向;但当冶金较差时,熔池难以获得基板的 $[001]$ 生长初始条件,晶体生长杂乱,取向差最大达到 56.5° 。所以,寻找合适的成

形参数,保证熔池与基板间的良好冶金结合是晶体外延生长的关键。

针对第二类缺陷,熔池中 Marangoni 对流能够扰动枝晶尖端的传热和传质过程,其溶质场的改变是枝晶偏转的主要原因^[25-26],并且对流越大,偏转角也增大^[27-28]。然而,图8(c)虚框内的晶体偏差角约为 0.89° 、 1.23° ,仍在 15° 以内,满足要求(工程上通常以 15° 作为单晶制作使用的判据^[29]),说明该熔池的对流较弱,不足以破坏晶体的原有生长特性。

针对第三类缺陷,即熔池顶部产生了柱状晶向等轴晶的转变(CET),从而生成了杂晶。Gäumann等^[30]建

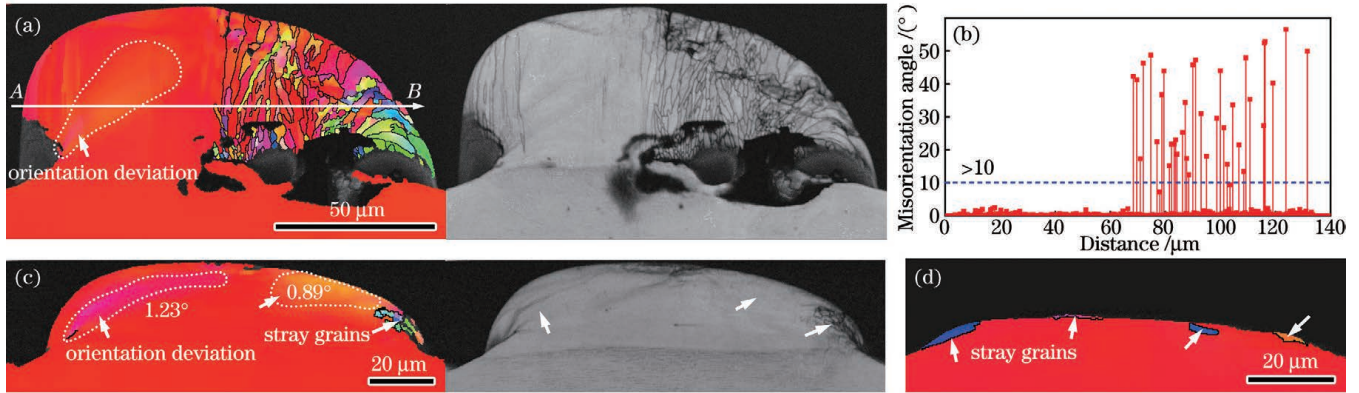


图 8 具有取向缺陷的熔池形貌。(a)245 W 激光功率、600 mm/s 扫描速度下的熔池晶体取向；(b)图 8(a)中 A 至 B 的晶界角差分布；(c)245 W 激光功率、800 mm/s 扫描速度下的熔池晶体取向；(d)275 W 激光功率、900 mm/s 扫描速度下的熔池晶体取向
Fig. 8 Morphologies of molten pools with orientation defects. (a) Crystal orientation of molten pool at laser power of 245 W and scanning speed of 600 mm/s; (b) distribution of grain boundary misorientation angle from A to B in Fig. 8(c); (c) crystal orientation of molten pool at laser power of 245 W and scanning speed of 800 mm/s; (d) crystal orientation of molten pool at laser power of 275 W and scanning speed of 900 mm/s

立的非平衡凝固条件与微观组织的关系判据为

$$\frac{G''}{V} = K_{\text{CET}} = a \left[\frac{-4\pi N_0}{\sqrt{3\ln(1-\phi)}} \cdot \frac{1}{n+1} \right]^n, \quad (2)$$

式中： G 为熔池温度梯度； V 为凝固速率； N_0 为单位体积内的形核位点数； ϕ 为等轴晶的体积分数； a 、 n 为与材料相关的参数。可以得出，当凝固条件满足 $G''/V > K_{\text{CET}}$ 时，理论上不发生 CET，即晶粒全部为柱状晶；但当 $G''/V < K_{\text{CET}}$ 时，将发生 CET，出现等轴晶缺陷。在 SLM 的熔池凝固过程中，随着固液界面由熔池底部向顶部推进，温度梯度逐渐减小，而凝固速率不断增大^[31]，使得 G''/V 逐渐减小，导致在凝固后期

容易产生 CET，出现晶体取向偏差，甚至杂晶等缺陷。此外，凝固界面前沿的枝晶碎片也能作为等轴晶的异质形核核心^[32]。然而，这类缺陷在多道多层的打印过程中可能较少，通过合理调控道-道间的搭接率和层-层的厚度可将此类杂晶再熔化、再凝固，实现晶粒典型的逐层外延生长。

3.3 微观组织

SRR99 合金铸态组织中含有大量细小均匀的 γ' -Ni₃(Al, Ti) 沉淀相^[33]，DD91 合金与其类似，其强化主要靠 γ 基体的固溶强化和 γ' 相的沉淀强化来实现。图 9 为激光功率为 260 W、扫描速度为 500 mm/s

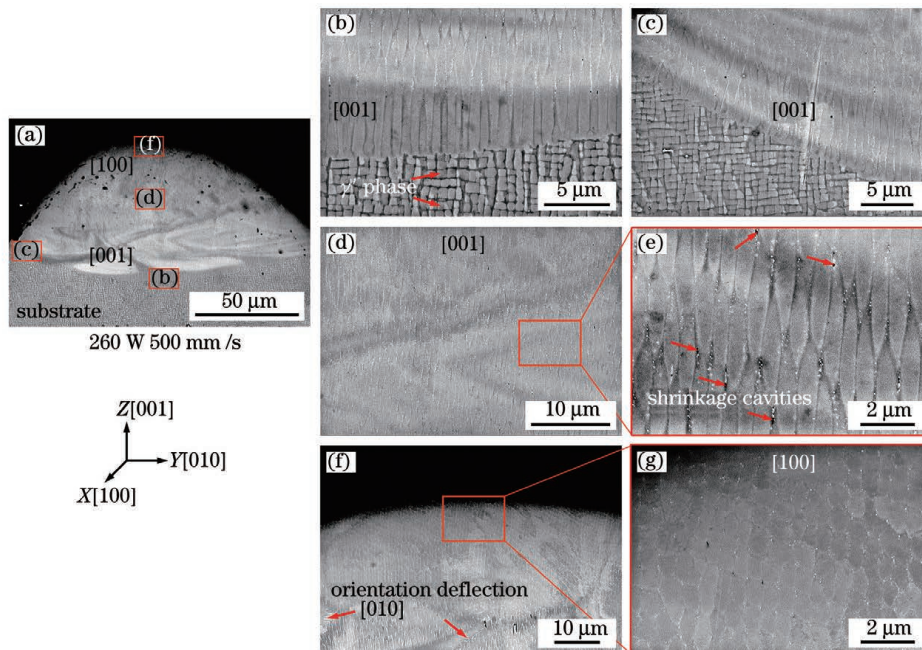


图 9 激光功率为 260 W、扫描速度为 500 mm/s 时的熔池形貌和组织。(a)熔池整个形貌；(b)熔池底部；(c)熔池两侧；(d)(e)熔池中部；(f)(g)熔池顶部

Fig. 9 Morphologies and microstructures of molten pool at laser power of 260 W and scanning speed of 500 mm/s. (a) Overall morphology of molten pool; (b) bottom morphology of molten pool; (c) morphology of both sides of molten pool; (d)(e) middle morphologies of molten pool; (f)(g) top morphologies of molten pool

时的熔池和基板电镜形貌和组织。熔池和基板的整体形貌如图9(a)所示,两者冶金结合良好。图9(b)~(g)分别对应熔池不同区域的显微形貌和微观组织。

在熔池底部和两侧,如图9(b)、(c)所示,大量近乎平行的柱状枝晶沿[001]生长,延续了基板的取向,一次枝晶臂间距仅为 $0.6\sim 0.8\ \mu\text{m}$,远低于定向凝固的(约 $289\ \mu\text{m}^{[34]}$),且没有二次枝晶臂。此外,从SRR99铸态基板上可以看到(箭头所指), γ 基体表面均匀分布且规则排列着大量的立方状 γ' 相,尺寸为 $0.4\sim 0.6\ \mu\text{m}$,然而在SLM的熔池内部却难以观察到 γ' 相。这可能由于熔池的凝固速度过快,Al来不及扩散与Ni结合形成 γ' 沉淀相,直接固溶到 γ 基体中, γ' 数量少;或者 γ' 虽能够形核,但来不及长大, γ' 尺寸小,难以通过SEM观察到。

在熔池中上部,如图9(d)、(e)所示,晶粒延续了熔池底部的[001]晶体取向定向生长,然而晶粒形态转变为纺锤状,长为 $3\sim 4\ \mu\text{m}$,宽为 $0.5\sim 0.6\ \mu\text{m}$ 。此外,在部分枝晶间也存在着细小的收缩孔洞缺陷,近似球形和长条形,宽约为 $0.1\ \mu\text{m}$,这些细孔主要是最后凝固的枝晶间缝隙没有液相及时补充造成的^[35]。

在熔池顶部,如图9(f)和(g)所示,晶粒转变为细小胞状结构,胞晶间距为 $0.6\sim 0.8\ \mu\text{m}$,意味着其生长方向由[001]转变为[100],并且局部区域存在少量[010]方向生长的晶体。这是由于此熔池较高,凝固末期热量自上而下传递至基板的距离变大,故热量主要沿扫描方向(平行于基板)传递,晶体的生长方向也转变为[100]。此外,依据3.2节的分析,此区域也极易发生CET形成等轴杂晶。因此,应优选合适工艺参数,尽可能减小熔池的高度,从而降低顶部到基板的传热距离,减少此类缺陷的产生。

4 结 论

通过激光选区熔化成形出DD91镍基单晶高温合金的单道试样,研究了激光功率和扫描速度对单条熔道的形貌、晶体取向和微观组织的影响规律,得到以下主要结论。

1) 当铺粉层厚为 $30\ \mu\text{m}$ 时,在激光功率为 $290\sim 305\ \text{W}$ 、扫描速度为 $500\sim 700\ \text{mm/s}$ 的条件下,熔道连续平稳、光滑平直,熔池扁平规则,其温度梯度方向更接近于 $[00\bar{1}]$,有利于熔池自上而下单向传热,为单晶组织的稳定生长提供保障。

2) 熔池与单晶基板间良好的冶金结合是晶体外延生长的关键,当熔道与基板未冶金结合时,熔池将难以获得基板初始取向,导致晶粒生长杂乱;个别熔池顶部和两侧存在少量等轴晶杂晶缺陷,这是凝固后期的温度梯度变低、凝固速率增大导致的。

3) 熔池内不同区域的晶体具有不同的特征。熔池底部和两侧的晶体延续了基板[001]外延生长,一次枝晶臂间距仅为 $0.6\sim 0.8\ \mu\text{m}$,远低于定向凝固的;熔

池中部晶体呈纺锤状,也延续了[001]取向生长,但枝晶间存在宽 $0.1\ \mu\text{m}$ 的凝固收缩孔洞;熔池顶部晶体为细小胞状结构,沿[100]方向生长,这是顶部热量沿扫描方向(平行于基板)传递导致的。

参 考 文 献

- [1] 李勇, 郑碰菊, 张建波, 等. 定向凝固技术的研究现状及发展趋势[J]. 材料导报, 2014, 28(23): 108-112.
Li Y, Zheng P J, Zhang J B, et al. Research progress and prospect of directional solidification technology[J]. Materials Reports, 2014, 28(23): 108-112.
- [2] 刘林, 孙德建, 黄太文, 等. 高梯度定向凝固技术及其在高温合金制备中的应用[J]. 金属学报, 2018, 54(5): 615-626.
Liu L, Sun D J, Huang T W, et al. Directional solidification under high thermal gradient and its application insuperalloys processing[J]. Acta Metallurgica Sinica, 2018, 54(5): 615-626.
- [3] 郭如峰, 刘林, 李亚峰, 等. 液态金属冷却法制备DD403合金过程温度场和晶粒组织的数值模拟[J]. 铸造, 2014, 63(2): 145-151.
Guo R F, Liu L, Li Y F, et al. Numerical simulation of temperature field and grain texture during casting single crystal superalloy DD403 with liquid metal cooling[J]. Foundry, 2014, 63(2): 145-151.
- [4] 滕庆, 李帅, 薛鹏举, 等. 激光选区熔化Inconel 718合金高温腐蚀性能[J]. 中国有色金属学报, 2019, 29(7): 1417-1426.
Teng Q, Li S, Xue P J, et al. High-temperature corrosion resistance of Inconel 718 fabricated by selective laser melting[J]. The Chinese Journal of Nonferrous Metals, 2019, 29(7): 1417-1426.
- [5] Gäumann M, Henry S, Cléton F, et al. Epitaxial laser metal forming: analysis of microstructure formation[J]. Materials Science and Engineering: A, 1999, 271(1/2): 232-241.
- [6] He P D, Webster R F, Yakubov V, et al. Fatigue and dynamic aging behavior of a high strength Al-5024 alloy fabricated by laser powder bed fusion additive manufacturing[J]. Acta Materialia, 2021, 220: 117312.
- [7] DebRoy T, Mukherjee T, Wei H L, et al. Metallurgy, mechanistic models and machine learning in metal printing[J]. Nature Reviews Materials, 2021, 6(1): 48-68.
- [8] 黄卫东, 林鑫, 陈静. 激光立体成形[M]. 西安: 西北工业大学出版社, 2007.
Huang W D, Lin X, Chen J. Laser solid forming[M]. Xi'an: Northwestern Polytechnical University Press, 2007.
- [9] Wang G W, Shen X F, Yang J L, et al. Microstructure evolution and tensile property of a first-generation single crystal superalloy fabricated by laser melting deposition[J]. Materials Research Express, 2020, 7(7): 076511.
- [10] Liang Y J, Li J, Li A, et al. Solidification path of single-crystal nickel-base superalloys with minor carbon additions under laser rapid directional solidification conditions[J]. Scripta Materialia, 2017, 127: 58-62.
- [11] Liang Y J, Li J, Li A, et al. Experimental optimization of laser additive manufacturing process of single-crystal nickel-base superalloys by a statistical experiment design method[J]. Journal of Alloys and Compounds, 2017, 697: 174-181.
- [12] 潘爱琼, 张辉, 王泽敏. 镍基单晶高温合金选区激光熔化成形工艺及组织[J]. 中国激光, 2019, 46(11): 1102007.
Pan A Q, Zhang H, Wang Z M. Process parameters and microstructure of Ni-based single crystal superalloy processed by selective laser melting[J]. Chinese Journal of Lasers, 2019, 46(11): 1102007.
- [13] Yang J J, Li F Z, Pan A Q, et al. Microstructure and grain growth direction of SRR99 single-crystal superalloy by selective laser melting[J]. Journal of Alloys and Compounds, 2019, 808:

- 151740.
- [14] Shrestha S, Chou K. An investigation into melting modes in selective laser melting of Inconel 625 powder: single track geometry and porosity [J]. *The International Journal of Advanced Manufacturing Technology*, 2021, 114(11/12): 3255-3267.
- [15] 袁伟豪, 陈辉, 魏青松. 反冲压力作用下激光选区熔化熔池热动力学行为[J]. *机械工程学报*, 2020, 56(7): 213-219.
Yuan W H, Chen H, Wei Q S. The role of recoil pressure in thermodynamic behaviors of molten pool during selective laser melting[J]. *Journal of Mechanical Engineering*, 2020, 56(7): 213-219.
- [16] Vaglio E, De Monte T, Lanzutti A, et al. Single tracks data obtained by selective laser melting of Ti6Al4V with a small laser spot diameter[J]. *Data in Brief*, 2020, 33: 106443.
- [17] Catchpole-Smith S, Aboulkhair N, Parry L, et al. Fractal scan strategies for selective laser melting of 'unweldable' nickel superalloys[J]. *Additive Manufacturing*, 2017, 15: 113-122.
- [18] 张洁, 李帅, 魏青松, 等. 激光选区熔化 Inconel 625 合金开裂行为及抑制研究[J]. *稀有金属*, 2015, 39(11): 961-966.
Zhang J, Li S, Wei Q S, et al. Cracking behavior and inhibiting process of Inconel 625 alloy formed by selective laser melting [J]. *Chinese Journal of Rare Metals*, 2015, 39(11): 961-966.
- [19] Hariharan A, Lu L, Risse J, et al. Misorientation-dependent solute enrichment at interfaces and its contribution to defect formation mechanisms during laser additive manufacturing of superalloys [J]. *Physical Review Materials*, 2019, 3(12): 123602.
- [20] Rong P, Wang N, Wang L, et al. The influence of grain boundary angle on the hot cracking of single crystal superalloy DD6[J]. *Journal of Alloys and Compounds*, 2016, 676: 181-186.
- [21] Tang Y T, Panwisawas C, Ghossoub J N, et al. Alloys-by-design: application to new superalloys for additive manufacturing [J]. *Acta Materialia*, 2021, 202: 417-436.
- [22] Wu Y C, San C H, Chang C H, et al. Numerical modeling of melt-pool behavior in selective laser melting with random powder distribution and experimental validation[J]. *Journal of Materials Processing Technology*, 2018, 254: 72-78.
- [23] 刘龙涛, 陈超越, 李霞, 等. 激光增材制造单晶高温合金研究进展[J]. *精密成形工程*, 2019, 11(4): 73-80.
Liu L T, Chen C Y, Li X, et al. Research progress in laser additive manufacturing technology of single crystal superalloy [J]. *Journal of Netshape Forming Engineering*, 2019, 11(4): 73-80.
- [24] 石德珂. *材料科学基础* [M]. 2 版. 北京: 机械工业出版社, 2003: 239-247.
Shi D K. *Fundamentals of materials science* [M]. 2nd ed. Beijing: China Machine Press, 2003: 239-247.
- [25] Tönhardt R, Amberg G. Phase-field simulation of dendritic growth in a shear flow [J]. *Journal of Crystal Growth*, 1998, 194(3/4): 406-425.
- [26] Wang G W, Liang J J, Zhou Y Z, et al. Variation of crystal orientation during epitaxial growth of dendrites by laser deposition [J]. *Journal of Materials Science & Technology*, 2018, 34(4): 732-735.
- [27] Murakami K, Aihara H, Okamoto T. Growth direction of columnar crystals solidified in flowing melt [J]. *Acta Metallurgica*, 1984, 32(6): 933-939.
- [28] Lu N N, Lei Z L, Yu X F, et al. Effects of melt convection on stray grain formation in single crystal superalloys during directed energy deposition [J]. *Additive Manufacturing*, 2021, 48: 102429.
- [29] 曹腊梅, 杨曦桥, 薛明, 等. 定向凝固过程中温度参数对含 Re 镍基单晶高温合金铸态组织的影响 [J]. *材料工程*, 2012, 40(10): 8-11.
Cao L M, Yang X Q, Xue M, et al. Influence of temperature parameters during directional solidification on structure of as-cast rhenium-containing Ni-base single crystal superalloy [J]. *Journal of Materials Engineering*, 2012, 40(10): 8-11.
- [30] Gäumann M, Bezençon C, Canalis P, et al. Single-crystal laser deposition of superalloys: processing-microstructure maps [J]. *Acta Materialia*, 2001, 49(6): 1051-1062.
- [31] 吴楷, 张敬霖, 吴滨, 等. 激光增材制造镍基高温合金研究进展 [J]. *钢铁研究学报*, 2017, 29(12): 953-959.
Wu K, Zhang J L, Wu B, et al. Research and development of Ni-based superalloy fabricated by laser additive manufacturing technology [J]. *Journal of Iron and Steel Research*, 2017, 29(12): 953-959.
- [32] 孙晓峰, 宋巍, 梁静静, 等. 激光增材制造高温合金材料与工艺研究进展 [J]. *金属学报*, 2021, 57(11): 1471-1483.
Sun X F, Song W, Liang J J, et al. Research and development in materials and processes of superalloy fabricated by laser additive manufacturing [J]. *Acta Metallurgica Sinica*, 2021, 57(11): 1471-1483.
- [33] 潘爱琼, 张莉, 王泽敏. 选区激光熔化 SRR99 高温合金的定向凝固组织及偏析 [J]. *激光与光电子学进展*, 2017, 54(10): 101409.
Pan A Q, Zhang L, Wang Z M. Directional solidification microstructure and segregation of SRR99 superalloys by selective laser melting [J]. *Laser & Optoelectronics Progress*, 2017, 54(10): 101409.
- [34] Hu S S, Yang W C, Li Z R, et al. Formation mechanisms and control method for stray grains at melt-back region of Ni-based single crystal seed [J]. *Progress in Natural Science: Materials International*, 2021, 31(4): 624-632.
- [35] Lu N N, Lei Z L, Hu K, et al. Hot cracking behavior and mechanism of a third-generation Ni-based single-crystal superalloy during directed energy deposition [J]. *Additive Manufacturing*, 2020, 34: 101228.

Single-Track Morphology, Crystal Orientation and Microstructure of DD91 Nickel-Based Single Crystal Superalloy Fabricated by Selective Laser Melting

Li Jikang¹, Zhang Zhenwu¹, Yang Yuanqi¹, Cai Chao¹, Li Wei^{2,3,4*}, Wei Qingsong^{1*}

¹ State Key Laboratory of Material Processing and Die & Mould Technology, School of Materials Science and Engineering, Huazhong University of Science and Technology, Wuhan 430074, Hubei, China;

² Key Laboratory of Metallurgical Equipment and Control Technology, Ministry of Education, Wuhan University of Science and Technology, Wuhan 430081, Hubei, China;

³ Hubei Key Laboratory of Mechanical Transmission and Manufacturing Engineering, Wuhan University of Science and Technology, Wuhan 430081, Hubei, China;

⁴ Precision Manufacturing Institute, Wuhan University of Science and Technology, Wuhan 430081, Hubei, China

Abstract

Objective Nickel-based single crystal superalloys have excellent high-temperature properties and are mainly used in the manufacture of aero-engine turbine blades. A high temperature gradient is the key to single crystal formation. Selective laser melting (SLM) is a kind of metal additive manufacturing, which uses a laser as the heat source to form the parts with fine metal powders layer by layer, especially the complex structures. The small laser spot (80–100 μm) has extremely high thermal density, which promotes a temperature gradient of 10^3 – 10^5 K/cm and a solidification rate of 10^5 – 10^7 K/s in the molten pool. In addition, a laser has obvious directional heat transfer characteristics, and the solidification heat can be directionally dissipated along the path from the molten pool to the substrate. Therefore, to explore the feasibility of single crystals fabricated by SLM, thirty-five single track samples are fabricated under different laser powers and scanning speeds. The geometric features, crystal orientation, and microstructures are first analyzed systematically. Then, the formation mechanisms of cracks and stray grains are discussed, which provides theoretical and technical reference for the preparation of large-scale single crystal structures by SLM.

Methods The particle size distribution of the gas-atomized DD91 nickel-based single crystal superalloy powder is in the range of 8.6–37.5 μm with an average of 20.4 μm . The SRR99 single crystal substrate prepared by directional solidification is tested by electron backscattered diffraction (EBSD) and it is found that the grain grows along the direction of [001], which meets the experimental needs. Before the experiment, the powder is placed in an oven at 80 $^{\circ}\text{C}$ for 10 h to remove moisture. The single crystal substrate is polished with sandpaper, and impurities such as abrasive debris are removed in an ultrasonic cleaning machine. DD91 alloy powder with a layer thickness of 30 μm is spread on the (001) crystal surface of the SRR99 single crystal substrate. A self-developed SLM equipment with a laser spot diameter of ~ 100 μm is used for the printing experiments. Thirty-five single-track samples with different parameters are fabricated on the substrate with a laser power of 245–305 W and a scanning speed of 500–1100 mm/s. Optical microscope (OM) is used to observe the surface morphologies of the single-tracks and evaluate the forming quality. Scanning electron microscope (SEM) is used to observe the microscopic morphologies and microstructures of powder and molten pools. ImageJ software is used to measure and analyze the geometric feature sizes of molten pools. EBSD is used to analyze the crystal orientation with a scanning step of 0.25 μm , and AztecCrystal software is used to process the collected data.

Results and Discussions When the line energy density is in the range of 414–580 $\text{J}\cdot\text{m}^{-1}$, excellent single-tracks could be obtained with clear surface contours, continuous flatness, and obvious metallic luster on the surface (Fig. 3). The shape of the molten pool is more regular and stable at a higher power and a lower speed, which could provide good geometric conditions for the epitaxial growth of single crystals. At a laser power of 290 W and scanning speeds of 1000 mm/s and 1100 mm/s, cracks perpendicular to the scanning direction are produced, running through the entire single-track. The dendrites are exposed to the crack section, leaving a wide irregular crack, which is the characteristic of a typical solidification crack, probably due to the excessive Al content of the alloy and the tearing of the liquid film between the dendrites under stress (Fig. 4). Most of the grains in the molten pool exhibit a very clear meritoric orientation, i.e., they can continue the orientation of the single crystal substrate and grow along [001] epitaxially. However, there are still crystal defects in some molten pools (Fig. 7). They can be divided into three categories: first, poor metallurgy between the molten pool and the single crystal substrate, resulting in disordered grain growth; second, during the growth of the crystal, its growth direction is shifted by a small angle, producing an orientation deviation due to the flow field in the molten pool; third, the columnar to equiaxed transition (CET) occurs at the top and sides of the

molten pool due to the reduced temperature gradient and the accelerated solidification rate at the late solidification stage, resulting in equiaxed stray grains (Fig. 8). At the bottom of the molten pool, near-parallel columnar dendrites grow along [001], continuing the orientation of the substrate without secondary dendrite arms. In the middle of the molten pool, the grains also grow and continue the [001] crystal orientation, however, the grain morphology changes to a spindle shape. At the top of the molten pool, the grain growth direction changes from [001] to [100] (Fig. 9). Due to the larger height of this molten pool, the distance of heat transfer to the substrate from top to bottom at the end of solidification becomes farther and the heat is mainly transferred along the scanning direction (parallel to the substrate). Suitable process parameters should be selected to minimize the height of the molten pool, thus to reduce the heat transfer distance from the top to the substrate and reduce the generation of such defects.

Conclusions Continuous, smooth, and straight single-tracks could be obtained within a fixed layer thickness of 30 μm , a laser power of 290–305 W and a scanning speed of 500–700 mm/s. The direction of the temperature gradient in the flat and regular molten pool is closer to $[00\bar{1}]$, which is more conducive to the unidirectional heat transfer from top to bottom in the molten pool, and provides a guarantee for the stable growth of the single crystal. A good metallurgical bond between the molten pool and the single crystal substrate is the key to the epitaxial growth of crystals. It is difficult to obtain the initial orientation of the substrate for the molten pool under poor metallurgical conditions, resulting in disordered crystal growth. Small angular orientation deviations occur due to the internal flow field. A small number of stray grains occur at the top and sides of individual molten pools, caused by the lower temperature gradient and the increased solidification rate in the later stages of solidification. The grains in different regions within the molten pools have different characteristics. Grains at the bottom and both sides of the molten pool can continue the substrate [001] epitaxial growth, and the primary dendrite arm spacing is only 0.6–0.8 μm , much lower than that of the directional solidification. Spindle-shaped grains occurring in the middle of the molten pool also continue the [001] orientation, but the solidification shrinkage holes with a width of 0.1 μm generate between the dendrites. At the top of the molten pool, the grains show a fine cellular structure, growing along the [100] direction, which is caused by the heat transfer along the scanning direction (parallel to the substrate). This study provides a process basis for the fabrication of large-size single crystals by SLM.

Key words laser technique; selective laser melting; DD91 alloy; nickel-based single crystal superalloy; single-track; crystal orientation; microstructure